Title

Computational Modeling of Ephaptic coupling in Myelinated and Unmyelinated Axon Bundles Using the EMI Framework

ISBN

9783031531446

Authors

Gatti, Alessandro

Nartallo-Kaluarachchi, Ramón

Uppal, Abhinav

et al.

Publication Date

2024

DOI

10.1007/978-3-031-53145-3_2

Alessandro Gatti, Ramón Nartallo-Kaluarachchi, Abhinav Uppal, Pietro Benedusi

Computational modeling of ephaptic coupling in myelinated and unmyelinated axon bundles using the EMI framework

SSCP 2023

September 1, 2023

Abstract This report examines the Extracellular-Membrane-Intracellular (EMI) framework for modeling action potentials along 3D axons. We investigate the effect of myelination and the potential for ephaptic coupling in this model. Additionally, we assess the convergence and stability of a range of Runge-Kutta time-stepping algorithms on simple geometries with manufactured solutions. We first analyze single axons and the influence of myelin on the speed of action potentials. Then, we use a 3D geometry of nine cylinders to represent an axonal bundle and study the induced potential in the central axon in both myelinated and unmyelinated cases. Finally, we discuss the biological implications of ephaptic coupling and the importance of 3D modeling for precise simulations of spiking neurons.

0.1 Introduction

Hodgkin and Huxley's 1952 work [16] was a pioneering effort to quantitatively describe the chemical processes that cause excitatory neurons to fire. Since then, a variety of alternative models, such as FitzHugh-Nagumo [9] and Hindmarsh-Rose [14] ODE models, have been developed to model excitable cells. The emergence of neural networks has further led to the modeling of neurons as single points in space with only time-dependent dynamics. In this report, we explore two biological scenarios in which spatial and temporal dynamics are necessary to accurately model the propagation and induction of action potentials. Specifically, we investigate the effects of myelination [13] and ephaptic coupling in axonal bundles [2]. To do this, we use the recent EMI model to incorporate spatial dynamics into a partial differential equation (PDE) framework [26].

0.1.1 Myelination

The myelin sheath is an extended and modified plasma membrane that is wrapped around the nerve axon in a spiral pattern [19]. It is derived from and is part of Schwann cells in the peripheral nervous system (PNS) and oligodendroglial cells in the central nervous system (CNS). Each myelin-generating cell provides myelin for only one segment of the axon. The nodes of Ranvier, which are short portions of the axon left uncovered, are essential for the functioning of myelin. This myelin sheath increases the resistance of the axonal membrane, lengthening its electrical space constant, and thus facilitating signal transmission along the axon. Additionally, myelin decreases the capacitance of the axonal membrane, so that less charge (in the form of Na^+) is required to depolarize the cell. Both of these effects increase the speed of action potential propagation.

0.1.2 Ephaptic coupling

The term *ephapse* was proposed in 1941 by Arvanitaki [3] to describe neural structures coming into contact or in close proximity, without coupling via anatomically differentiated synapses. Where Arvanitaki had been studying an experimental preparation with two giant axons (from *Sepia officinalis*) forming an ephapse by making the axons touch (for 5 mm in 4 to 5 cm long axons), the term ephaptic coupling has since come to describe short-range coupling between noncontiguous neuronal membranes [17], alternatively described as 'electric field effects' [1].

Similarly to how spiking individual neurons can give rise to extracellular action potentials, network-level activity can alter the local electric environment in nervous tissue. This spatiotemporal variation in extracellular potential and its gradient electric field feed back into the same network, inducing ephaptic coupling [2]. This electric ephatic coupling can be contrasted with ionic ephaptic coupling, where local changes in extracellular ion concentrations can alter Nernst potentials [8].

Although ephaptic coupling between neurons can be considered a weak effect compared to chemical or electrical synapses (measurements of endogenous electric fields are on the order of a few mV/mm, see [22] for a summary of experimental data), it can still have network-level implications in healthy and pathological nervous tissue [1]. For instance, weak electric fields can entrain slow neocortical oscillations [10]. Additionally, mathematical models of ephaptic coupling in axon bundles show induced synchronization of firing activity [4] and modulation of transmission delays [24].

In pathological scenarios, ephatic entrainment has been implicated in neurodegenerative disease models considering damaged neurons [7]. Ephaptic coupling is also hypothesized to play a role in pathologies resulting from demyelination of cranial nerves under compression, such as trigeminal neuralgia (facial pain) through the fifth cranial nerve [11] and vestibular paroxysmia (short episodic vertigo) from the eighth cranial nerve ([6], [18]).

Thus, studying ephaptic coupling can improve our understanding of network-level feedback under healthy and pathological conditions. Modeling studies of ephaptic coupling also offer the translational benefit of providing an evaluation framework in the design of exogenous (transcranial) stimulation protocols [22]. Given the key role of extracellular potentials in ephaptic coupling, here we extend previous work on modeling axon bundles using the EMI framework [8] by contrasting unmyelinated and myelinated axons in a bundle.

0.2 Methods

0.2.1 The EMI model

The EMI model is a PDE framework that has recently been developed to simulate excitable cells, such as neurons and cardiac cells, from the first principles [26]. It divides the extracellular space, the cell membrane, and the intracellular space into distinct components. When both spatial and temporal dynamics are taken into account, it is suitable for modeling the effects of myelination and ephaptic coupling.

For a single cell, denoted Ω_i, surrounded by an extracellular domain, Ω_e, the EMI model is given by the following coupled PDE-ODE,

$$\begin{aligned}
\boldsymbol{\nabla} \cdot \sigma_i \boldsymbol{\nabla} u_i &= f, && \text{in} \quad \Omega_i, \\
\boldsymbol{\nabla} \cdot \sigma_e \boldsymbol{\nabla} u_e &= g, && \text{in} \quad \Omega_e, \\
\sigma_e \boldsymbol{\nabla} u_e \cdot \mathbf{n}_e &= -\sigma_i \boldsymbol{\nabla} u_i \cdot \mathbf{n}_i \equiv I_m, && \text{at} \quad \Gamma, \\
v &= u_i - u_e, && \text{at} \quad \Gamma, \\
\frac{\partial v}{\partial t} &= \frac{1}{C_m}(I_m - I_{ion}), && \text{at} \quad \Gamma,
\end{aligned} \tag{0.1}$$

where u_i, u_e, and v are intracellular, extracellular, and membrane potentials, respectively, which are commonly given in mV. Furthermore, σ_i and σ_e are intracellular and extracellular conductances, respectively (typically in mS/cm), C_m is the membrane capacitance (typically in $\mu F/cm^2$), and Γ denotes the cell membrane. $\mathbf{n_i}$ and $\mathbf{n_e}$ represent the outward-pointing normal vectors. The ionic currents through channels, pumps, and exchangers at the membrane are denoted by I_{ion} and are typically given in $\mu A/cm^2$. A schematic representation of the model domain is given in Fig. 0.1.

We assumed that the external boundary $\partial\Omega_e$ is insulated, which leads to the following Neumann boundary condition

$$\sigma_e \boldsymbol{\nabla} u_e \cdot \mathbf{n}_e = 0, \qquad \text{at} \quad \partial\Omega_e. \tag{0.2}$$

0.2.2 Numerical methods

0.2.2.1 Multi-dimensional primal formulation of the EMI model

In order to numerically integrate the EMI model, we derive a weak formulation [26]. In particular, we use the multi-dimensional primal formulation which is expressed as follows: find $u_i \in V_i = H^1(\Omega_i)$, $u_e \in V_e = H^1(\Omega_e)$, $I_m \in Q^* = H^{-1/2}(\Gamma)$ such that

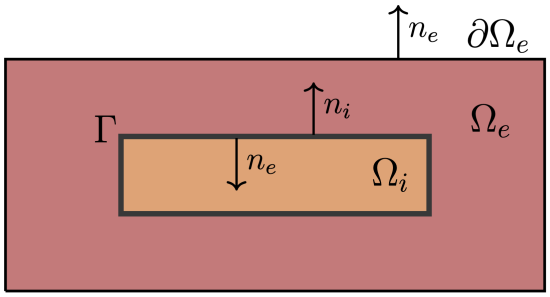

Fig. 0.1: Illustration of an EMI model domain consisting of an extracellular domain, Ω_e, a cell membrane, Γ, and an intracellular domain, Ω_i. $\mathbf{n_e}, \mathbf{n_i}$ represent normal vectors and $\partial\Omega_e$ represents the boundary of the extracellular space.

$$\begin{aligned}
\int_{\Omega_i} \sigma_i \nabla u_i \cdot \nabla v_i dx - \int_\Gamma I_m v_i ds &= \int_{\Omega_i} f v_i dx, \\
\int_{\Omega_e} \sigma_e \nabla u_e \cdot \nabla v_e dx - \int_\Gamma I_m v_e ds &= \int_{\Omega_i} g v_e dx, \\
\int_\Gamma -u_e j_m ds + \int_\Gamma u_i j_m ds - \int_\Gamma \Delta t C_m^{-1} I_m j_m ds &= \int_\Gamma h j_m ds,
\end{aligned} \tag{0.3}$$

for all the test functions $v_i \in V_i$, $v_e \in V_e$ and $j_m \in Q^*$ [26]. In this formulation, the time-dependent equations are discretized according to an implicit Euler scheme. The known right-hand side h combines the previous transmembrane potential solution, v_0, and the evaluation of the ionic current, I_{ion}, into $h \equiv v_0 - C_m^{-1} \Delta t I_{ion}$. However, as discussed in the following section, this final equation can be modified according to any time discretization.

0.2.2.2 Runge-Kutta time-stepping in the EMI model

As discussed above, the derivation of the weak formulation requires a choice of time discretization. Depending on the choice of the time-stepping algorithm, the final equation will differ. We consider the well-studied Runge-Kutta (RK) methods, a family of classical ODE integrators [12]. For a homogeneous differential equation of the form

$$\frac{dy}{dt} = f(y(t)), \tag{0.4}$$

an s-order RK scheme is a one-step method of the following form,

$$y_{n+1} = y_n + h \sum_{i=1}^{s} b_i k_i, \tag{0.5}$$

where,

$$k_1 = f(y_n), \tag{0.6}$$

$$\vdots$$

$$k_s = f(y_n + h \sum_{j=1}^{s} a_{ij} k_j). \tag{0.7}$$

Thus, the method is uniquely defined by the matrix vector pair $\boldsymbol{A}, \boldsymbol{b}$, where $\boldsymbol{A} = (a_{ij})$ and $\boldsymbol{b} = (b_1, ..., b_s)$. We can also define the vector $\boldsymbol{k} = (k_1, ..., k_2)$. To make this method consistent with the order s, certain conditions on $\boldsymbol{A}, \boldsymbol{b}$ must be satisfied, limiting the number of RK methods for each given order. When $\boldsymbol{A}$ is lower triangular with zero diagonal, the method is explicit; otherwise, it is implicit. We investigate the form of final EMI equation for a generalized RK scheme for both the passive and Hodgkin-Huxley conductance dynamics.

0.2.2.3 The passive conductance EMI model

We consider the time-dependent equation from the EMI model with passive conductance, corresponding to $I_{ion}(v) = v$ [26],

$$\frac{dv}{dt} = \frac{1}{C_m} \left(I_m - v(t) \right). \tag{0.8}$$

Considering an RK method of order s, we discretise this equation as,

$$v_{t+1} = v_t + h \sum_{i=1}^{s} b_i k_i, \tag{0.9}$$

$$= v_t + h \boldsymbol{b}^\top \boldsymbol{k}. \tag{0.10}$$

We further notice that

$$k_i = \frac{1}{C_m} (I_m - v_t - h \sum_{j=1}^{s} a_{ij} k_j), \tag{0.11}$$

which we write in vector notation as,

$$\boldsymbol{k} = \frac{1}{C_m} (I_m - v_t) \boldsymbol{u} - h \boldsymbol{A} \boldsymbol{k}, \tag{0.12}$$

where $\boldsymbol{u}$ is a s-vector of 1s. Defining $\beta = \frac{h}{C_m}$ and $\boldsymbol{I}$ to be the s-dimensional identity matrix, we assume $\boldsymbol{I} + \beta\boldsymbol{A}$ to be invertible and write $\boldsymbol{k}$ explicitly as

$$\boldsymbol{k} = \frac{1}{C_m}(I_m - v_t)(\boldsymbol{I} + \beta\boldsymbol{A})^{-1}\boldsymbol{u}. \tag{0.13}$$

As such, our RK scheme can be written as

$$v_{t+1} = (1 - \beta\boldsymbol{b}^\top(\boldsymbol{I} + \beta\boldsymbol{A})^{-1}\boldsymbol{u})v_t + \beta\boldsymbol{b}^\top(\boldsymbol{I} + \beta\boldsymbol{A})^{-1}\boldsymbol{u}I_m. \tag{0.14}$$

According to the weak formulation of the EMI model, this yields conservation law,

$$\begin{aligned}\int_\Gamma u_i \, ds - \int_\Gamma u_e \, ds - \beta\boldsymbol{b}^\top(\boldsymbol{I} + \beta\boldsymbol{A})^{-1}\boldsymbol{u} \int_\Gamma I_m \, ds \\ = (1 - \beta\boldsymbol{b}^\top(\boldsymbol{I} + \beta\boldsymbol{A})^{-1}\boldsymbol{u}) \int_\Gamma v_t \, ds.\end{aligned} \tag{0.15}$$

Given the Butcher tableau, $(\boldsymbol{A}, \boldsymbol{b})$, one can use this formulation to calculate the function,

$$g_{\mathrm{RK}}(\beta) = \beta\boldsymbol{b}^\top(\boldsymbol{I} + \beta\boldsymbol{A})^{-1}\boldsymbol{u}, \tag{0.16}$$

which can then be used to implement any RK scheme on the EMI model. Furthermore, we notice that $g_{\mathrm{RK}}(\beta)$ is related to the well-studied stability function of the RK family, which is defined [12],

$$R(z) = 1 + z\boldsymbol{b}^\top(\boldsymbol{I} - z\boldsymbol{A})^{-1}\boldsymbol{u}, \tag{0.17}$$

namely, the relation is,

$$g_{\mathrm{RK}}(\beta) = 1 - R(-\beta), \tag{0.18}$$

yielding conservation law,

$$\int_\Gamma u_i \, ds - \int_\Gamma u_e \, ds + (R(-\beta) + 1) \int_\Gamma I_m \, ds = R(-\beta) \int_\Gamma v_t \, ds. \tag{0.19}$$

The stability function can be written as

$$R(z) = \frac{\det(\boldsymbol{I} - z\boldsymbol{A} + z\boldsymbol{u}\boldsymbol{b}^\top)}{\det(\boldsymbol{I} - z\boldsymbol{A})}, \tag{0.20}$$

where for explicit scheme, due to their lower triangularity, the denominator is 1. Therefore, for explicit schemes, the stability function R and therefore g_{RK} is a polynomial of degree s, which we denote $p_s(\beta)$ that has form,

$$p_s(\beta) = \sum_{n=1}^{s} (-1)^{n+1}\beta^n\Theta(\boldsymbol{A}, \boldsymbol{b}, n), \tag{0.21}$$

with,

$$\Theta(\boldsymbol{A}, \boldsymbol{b}, n) = \sum_{i_0=n}^{s} b_{i_0} \sum_{i_1=n-1}^{i_0-1} a_{i_0,i_1} \cdots \sum_{i_k=n-k}^{i_{k-1}-1} a_{i_{k-1},i_k} \cdots \sum_{i_{n-1}=n-1}^{i_{n-2}-1} a_{i_{n-2},i_{n-1}}, \quad (0.22)$$

for $n = 2, ..., s$ and extended to $n = 1$ by,

$$\Theta(\boldsymbol{A}, \boldsymbol{b}, 1) = \sum_{i_0=1}^{s} b_{i_0} \quad (0.23)$$

This yields conservation law,

$$\int_\Gamma u_i \, ds - \int_\Gamma u_e \, ds - p_s(\beta) \int_\Gamma I_m \, ds = (1 - p_s(\beta)) \int_\Gamma v_t \, ds. \quad (0.24)$$

Following this process, we can derive the functions g_{RK} associated with a range of explicit and implicit RK schemes. In addition, we note that for explicit RK schemes

Table 0.1: Common Runge-Kutta schemes and the associated functions $g_{\mathrm{RK}}(\beta)$.

Scheme	Abbreviation	Order	Implicit/Explicit	$g_{\mathrm{RK}}(\beta)$
Explicit Euler	EE	1	E	β
Explicit Mid-point	EMP	2	E	$\beta - \frac{\beta^2}{2}$
Runge-Kutta 4	RK4	4	E	$\beta - \frac{\beta^2}{2} + \frac{1}{6}\beta^3 - \frac{1}{24}\beta^4$
Implicit Euler	IE	1	I	$\frac{\beta}{1+\beta}$
Trapezoidal Rule	TPR	2	I	$\frac{\beta}{2} + \frac{\beta-\beta^2}{2+\beta}$
Exponential function	EF	$p \in \mathbb{N}$	E	$1 - e^{-\beta}$

of order p, we have the following approximation,

$$R(z) = 1 + z + \frac{z^2}{2!} + \frac{z^3}{3!} + ... + \frac{z^p}{p!} + O(z^{p+1}), \quad (0.25)$$

therefore $R(z) = e^z + O(z^{p+1})$. Using this property, we can define the following scheme that approximates any explicit, p-order RK scheme to order p,

$$\int_\Gamma u_i \, ds - \int_\Gamma u_e \, ds + (e^{-\beta} + 1) \int_\Gamma I_m \, ds = e^{-\beta} \int_\Gamma v_t \, ds, \quad (0.26)$$

which is referred to in Table 0.1 as "Exponential function" (EF). This scheme represents the exact solution of the linear time-dependent equation.

As shown above, using both higher-order and implicit schemes in the passive conductance model can be done via direct calculation, and therefore at no additional computational cost.

0.2.2.4 Numerical convergence of RK schemes

In order to compare the convergence and stability of the different RK schemes, we consider the simple square unit domain shown in Fig. 0.2.

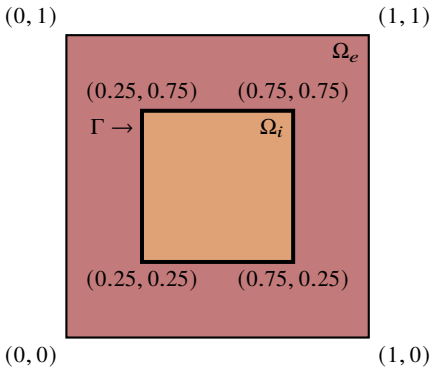

Fig. 0.2: Domain of integration. $\Omega_e, \Omega_i, \Gamma$ represent the extracellular space, the intracellular space and the membrane, respectively.

Using the manufactured solution method [25], we define the source functions

$$f = f(x, y, t) = -8\pi^2 \sin(2\pi x) \sin(2\pi y)(1 + e^{-t}), \tag{0.27}$$

$$g = g(x, y, t) = -8\pi^2 \sin(2\pi x) \sin(2\pi y). \tag{0.28}$$

In this case, the exact solution is given by,

$$u_i(x, y, t) = (1 + e^{-t}) \sin(2\pi x) \sin(2\pi y), \tag{0.29}$$

$$u_e(x, y, t) = \sin(2\pi x) \sin(2\pi y), \tag{0.30}$$

$$v(x, y, t) = e^{-t} \sin(2\pi x) \sin(2\pi y). \tag{0.31}$$

We calculate the L^2 error between the numerical solutions, $\tilde{u}_i^{N,\Delta t}, \tilde{u}_e^{N,\Delta t}, \tilde{v}^{N,\Delta t}$, using the finite element method (FEM) and the exact solutions above. We present the two error terms,

$$e_u^{N,\Delta t} = \sqrt{||u_i - \tilde{u}_i^{N,\Delta t}||^2 + ||u_e - \tilde{u}_e^{N,\Delta t}||^2}, \tag{0.32}$$

$$e_v^{N,\Delta t} = \sqrt{||v - \tilde{v}^{N,\Delta t}||^2}. \tag{0.33}$$

We assess the convergence with respect to both temporal and spatial resolution. For the spatial convergence test, we fix $\Delta t = 0.01/64$ and vary the mesh resolution parameter, $N = 16, 32, ..., 256$, which equals the number of intervals in each direction of spatial discretisation of the domain, as shown in Fig. 0.5. For the temporal resolution, we fix $N = 512$ and perform two experiments. Firstly, we use $\Delta t = 0.01/n$ for $n = 0.1, 0.5, 1, 2, 4, 8, 16, 32$, as shown in Fig. 0.6.

0.2.2.5 The active conductance model

For the EMI model with active conductance, the time-dependent equation becomes [26],

$$\frac{dv}{dt} = \frac{1}{C_m}\left(I_m - I_{\text{ion}}(v(t))\right), \tag{0.34}$$

where $I_{\text{ion}}(v(t))$ is a non-linear function, for example of Hodgkin-Huxley type. In this case, explicit expressions cannot be derived when applying RK schemes. Given an implicit RK scheme with Butcher tableau, $(\boldsymbol{A}, \boldsymbol{b})$, the scheme is again,

$$v_{t+1} = v_t + h\sum_{i=1}^{s} b_i k_i, \tag{0.35}$$

$$= v_t + h\boldsymbol{b}^\top \boldsymbol{k}. \tag{0.36}$$

However, the equations for k_i yield a non-linear system of equations to be solved at each time-step,

$$k_i = \frac{1}{C_m}(I_m - I_{\text{ion}}(v_t - h\sum_{j=1}^{s} a_{ij}k_j)), \tag{0.37}$$

which we write in vector notation as,

$$\boldsymbol{k} = \frac{1}{C_m}(I_m - F_{\text{ion}}(v_t, \boldsymbol{A}, \boldsymbol{k})), \tag{0.38}$$

where,

$$F_{\text{ion}}(v_t, \boldsymbol{A}, \boldsymbol{k}) = \begin{pmatrix} I_{\text{ion}}(v_t + \boldsymbol{e}_1^\top \boldsymbol{A}\boldsymbol{k}) \\ \vdots \\ I_{\text{ion}}(v_t + \boldsymbol{e}_s^\top \boldsymbol{A}\boldsymbol{k}) \end{pmatrix}, \tag{0.39}$$

where $\{\boldsymbol{e}_i\}_{i=1}^s$ are the standard basis vectors in $\mathbb{R}^s$.

Most frequently, one considers an active conductance of Hodgkin-Huxley type [16],

$$I_{\text{ion}}(v) = g_{\text{Na}}(v)(v - E_{\text{Na}}) + g_{\text{K}}(v)(v - E_{\text{K}}) + g_{\text{L}}(v)(v - E_{\text{L}}) + g(v)(v - E_{\text{Na}}), \tag{0.40}$$

where the gating variables, g_{ion}, for each ion, are non-linear functions of v given by the solution to an ODE. This form allows us to define semi-implicit schemes for this model. At each time step, the gating variables are updated according to a numerical method, typically the Rush-Larsen method [23]. To define a semi-implicit scheme, we update the gating variables with membrane potential v_t rather than the value $v_t + h\sum_{j=1}^s a_{ij}k_j$. This now yields a simplified system of equations for k_i,

$$\begin{aligned} k_i = \frac{1}{C_m}[I_m &- g_{\text{Na}}(v_t)(v_t + h\sum_{j=1}^s a_{ij}k_j - E_{\text{Na}}) - g_{\text{K}}(v_t)(v_t + h\sum_{j=1}^s a_{ij}k_j - E_{\text{K}}) \\ &- g_{\text{L}}(v_t)(v_t + h\sum_{j=1}^s a_{ij}k_j - E_{\text{L}}) - g(v_t)(v_t + h\sum_{j=1}^s a_{ij}k_j - E_{\text{Na}})], \end{aligned} \tag{0.41}$$

which is linear. In vector notation, the system becomes

$$\boldsymbol{k} = \frac{1}{C_m}[I_m - I_{\text{ion}}(v_t)]\boldsymbol{u} - \beta G\boldsymbol{A}\boldsymbol{k}, \tag{0.42}$$

where $G = g_{\text{Na}}(v_t) + g_{\text{K}}(v_t) + g_{\text{L}}(v_t) + g(v_t)$. This has solution,

$$\boldsymbol{k} = \frac{1}{C_m}[I_m - I_{\text{ion}}(v_t)](\boldsymbol{I} + \beta G\boldsymbol{A})^{-1}\boldsymbol{u}. \tag{0.43}$$

Thus, the scheme becomes as follows:

$$v_{t+1} = v_t + \beta\boldsymbol{b}^\top[I_m - I_{\text{ion}}(v_t)](\boldsymbol{I} + \beta G\boldsymbol{A})^{-1}\boldsymbol{u}. \tag{0.44}$$

Under the weak formulation this gives us conservation law,

$$\begin{aligned} \int_\Gamma u_i\, ds - \int_\Gamma u_e\, ds - \beta\boldsymbol{b}^\top(\boldsymbol{I} + \beta G\boldsymbol{A})^{-1}\boldsymbol{u}\int_\Gamma I_m\, ds \\ = \int_\Gamma v_t - I_{\text{ion}}(v_t)\boldsymbol{b}^\top(\boldsymbol{I} + \beta G\boldsymbol{A})^{-1}\boldsymbol{u}\, ds. \end{aligned} \tag{0.45}$$

However, this inverse matrix that must be calculated equates to solving a linear system at each time step.

0.2.3 Model setup and geometries

We employ the multi-dimensional EMI formulation (eq. 0.1) with an implicit Euler scheme (eq. 0.4). We use a Hodgkin-Huxley active conductance model [16] integrated with a Rush-Larsen scheme [23]. The source terms f and g in eq. 0.1 are set to 0 [26].

The model parameters were chosen as shown in Table 0.2. The conductance values for the unmyelinated axons correspond to the giant squid axon [16]. For the myelinated axons, we scaled the corresponding unmyelinated conductances such that the total number of ion channels would match for the two axon types. The axon length, radii, and node lengths were chosen to make the geometry and results easier to visualize. The synaptic conductance $g(v_t)$ in I_{ion} represents a stimulation current applied to a synapse of length l_{node} on one edge of unmyelinated and myelinated axons.

0.2.3.1 Single axon with and without myelination

Fig. 0.3 illustrates the geometries we employed in our simulation to compare the velocity of the action potential in a single axon for the unmyelinated (a) and myelinated (b) scenarios. Table 0.2 contains the parameters used for the axons.

Table 0.2: Parameters used for single axon simulations with and without myelin.

Parameter	**Value**	
	Unmyelinated	Myelinated
Axon length L (mm)	10	10
Intracellular radius r_{in} (mm)	0.2	0.2
Extracellular radius r_{ex} (mm)	1	1
Myelin thickness t_{myel} (mm)	–	0.2
Number of nodes of Ranvier	–	10
Length of node l_{node} (mm)	–	0.1
Internodal distance $l_{myel}(mm)$	–	1
$\bar{g}_L(mS/cm^2)$	0.3	3
$\bar{g}_{Na}(mS/cm^2)$	120	1200
$\bar{g}_K(mS/cm^2)$	36	360
$E_L(mV)$	-54.38	-54.38
$E_{Na}(mV)$	54.8	54.8
$E_K(mV)$	-88.98	-88.98

0.2.3.2 Axon bundle

For our simulations considering bundles of unmyelinated axons, we arranged nine axons in a 3×3 grid. A cross-section showing this spatial arrangement is depicted

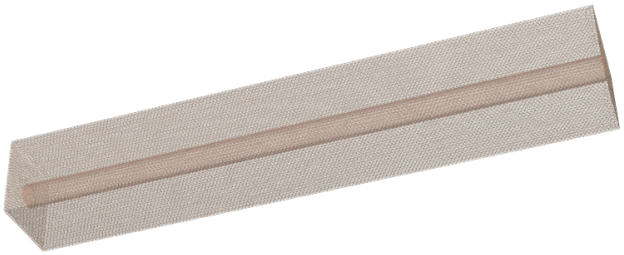

(a) *Unmyelinated axon*

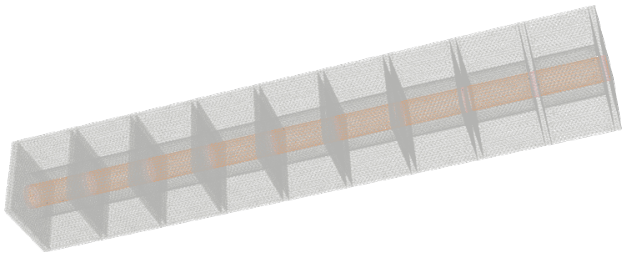

(b) *Myelinated axon*

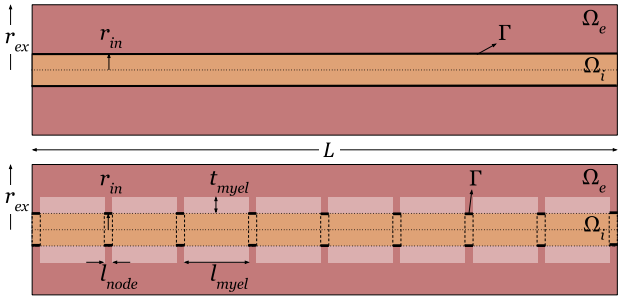

(c) *Longitudinal sections of unmyelinated (top) and myelinated (bottom) axons. Membrane boundaries shown as thick lines.*

Fig. 0.3: ParaView renders of the `gmsh` geometries for (a) unmyelinated, and (b) myelinated single axons, where (c) shows a schematic representation of both axon types using parameters from Table 0.2.

in Fig. 0.4. Each axon in the bundle was matched to use the same parameters and geometries as the single axon simulations described previously. The same arrangement and parameter matching to single axon simulations was also applied to a 3×3 bundle of myelinated axons.

For both the unmyelinated and myelinated axon bundles, the eight axons on the periphery were stimulated using synapses of length l_{node} (as in the single axon simulations), while the central axon in the bundle was not stimulated externally.

Membrane voltage changes in this central axon were examined to look for evidence of ephatic coupling.

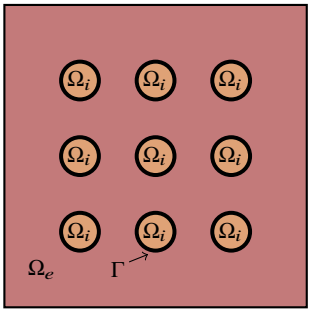

Fig. 0.4: Arrangement of nine axons forming a bundle. Ω_i denotes the intracellular space of each axon, Ω_e denotes the extracellular space, and Γ denotes the membranes.

0.3 Results

0.3.1 Convergence

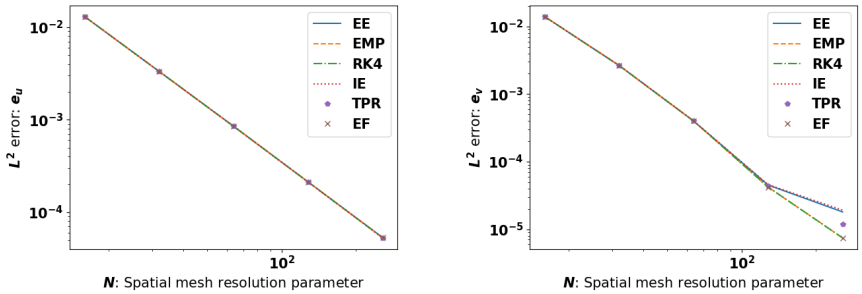

Fig. 0.5: Convergence with respect to mesh size with fixed time-step. Left: e_u Right: e_v.

Firstly, we consider the convergence results for the square-in-square, passive conductance, manufactured solution discussed previously. We integrate the system using FeNICS and the RK schemes listed in Table 0.1. In Fig. 0.5, we display the error for a sequence of increasing spatial (mesh) resolutions for both the intra-extracellular potential and the membrane potential. As shown, all the methods converge comparably with respect to mesh resolution, as they only modulate the time-stepping error. Next,

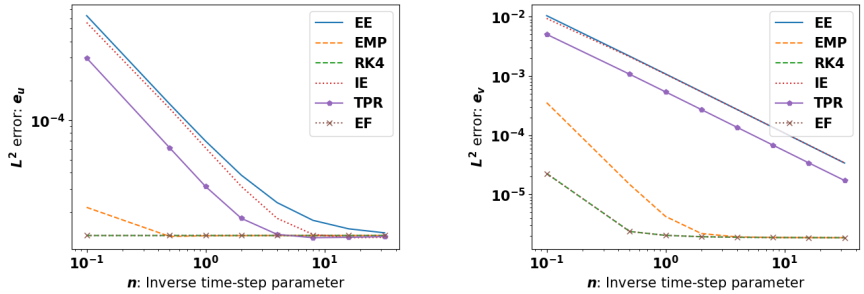

Fig. 0.6: Convergence with respect to temporal resolution for small time-steps and fixed mesh size. Left: e_u Right: e_v.

we consider a series of decreasing time steps. As can be seen in Fig. 0.6, higher-order methods are limited by spatial discretisation, but all methods appear to converge to the exact solution. It is clear that the higher-order methods, EMP, RK4 and TPR have lower errors than the first-order methods EE and IE. For these higher-order methods, in order to assess their convergence and their stability, we find the time steps at which they obtain similar error values. By increasing the time-steps so dramatically, we can limit the effect of the spatial discretisation error and compare the methods more effectively. As shown in Table 0.3, the least stable of the higher order methods

Table 0.3: Errors for large time-steps for higher order RK schemes.

Δt	**RK4**		Δt	**EMP**		Δt	**TPR**	
	e_u	e_v		e_u	e_v		e_u	e_v
2.5	1.03×10^{-5}	5.62×10^{-6}	1.6	1.03×10^{-5}	2.15×10^{-4}	3.0	1.60×10^{-5}	2.50×10^{-4}
2.6	2.99×10^{-5}	4.70×10^{-4}	1.8	1.64×10^{-5}	2.15×10^{-4}	3.2	1.30×10^{-4}	2.17×10^{-3}
2.7	1.74×10^{-3}	2.90×10^{-2}	2.0	1.65×10^{-1}	2.78	3.4	1.12×10^{-3}	1.87×10^{-2}

is EMP, followed by RK4 and finally TPR, the implicit scheme. Importantly, the higher order explicit schemes had much lower error yet are less stable. This means that, depending on the constraints of the particular problem, one should opt for an implicit scheme for greater stability or an explicit scheme for greater accuracy.

0.3.2 Speed of action potential propagation in single axons

We conducted a simulation to compare the propagation speed of an action potential in a myelinated axon with that of an unmyelinated one. Fig. 0.7 shows the membrane potential in both cases recorded at a single point on the membrane and at the end of

the axon. The action potential profile is similar in both cases. The key difference is that the potential propagates faster in the myelinated axon; therefore, it arrives at the end of the axon earlier, as shown in Fig. 0.7.

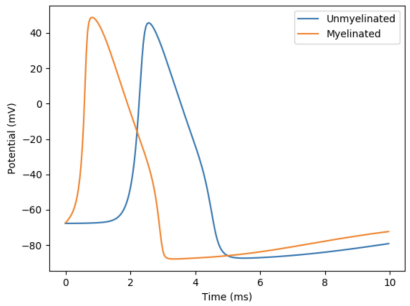

Fig. 0.7: Potential of myelinated and unmyelinated axons over time measured at the node located at the end of the axon membrane.

Our simulation supports the biological theory that argues that myelination causes faster propagation of action potential [21]. This further validates this approach to modeling myelination by modulating the conductance values in the nodes of Ranvier.

0.3.3 Ephaptic coupling in unmyelinated and myelinated axon bundles

Next, we simulate the 9-cylinder axonal bundle with myelinated and unmyelinated axons, while stimulating only the 8 peripheral axons. We then measured the induced activity in the unstimulated central axon.
In Fig. 0.8 (a), we show that in the unmyelinated case, ephaptic coupling did occur as an action potential was induced in the central axon. There is a noticeable time-lag between the spike in the peripheral and central axons. In the myelinated case, shown in Fig. 0.8 (b), ephaptic coupling also occurred with an induced potential in the central axon. There is no such time-lag in the case of the myelinated axons. The different profiles of the induced action potentials in each case are highlighted in Fig. 0.8 (c), which shows the unmyelinated and myelinated central axons side by side.
Interestingly, in our simulations we have observed a backpropagation phenomenon in the central unmyelinated axon as one can see from Fig. 0.9.

Our simulations show that ephaptic coupling is possible in the EMI model, for both myelinated and unmyelinated axons. Furthermore, we have shown that myelination severely increases the speed of the propagation of action potentials under direct stimulation and indirect induction.

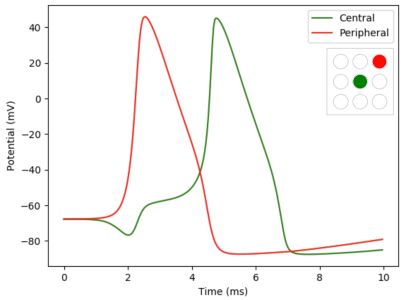

(a) *Comparison between the action potential of the central and peripheral axon in the unmyelinated case.*

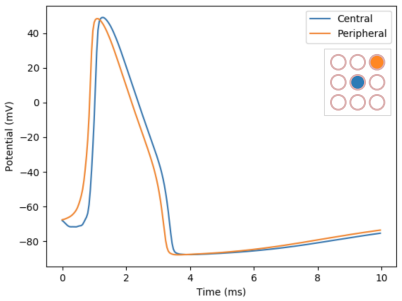

(b) *Comparison between the action potential of the central and peripheral axon in the myelinated case.*

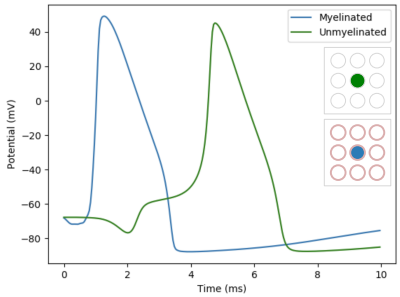

(c) *Comparison between the action potential of central axons in the unmyelinated and myelinated cases.*

Fig. 0.8: Plot showing the action potentials induced in the central axon alongside (a chosen) peripheral axon in both the myelinated and unmyelinated cases.

0.4 Discussion

In this report, we presented a computational approach to modeling myelination and ephaptic coupling of axons using the EMI framework [26]. As part of this analysis, we studied a range of time-stepping algorithms for both the passive and the Hodgkin-Huxley conductance models, obtaining an analytical expression for the weak formulation for generalized RK schemes. As a result, we can integrate the EMI model with any RK scheme. We concluded that higher-order schemes are advantageous in terms of both stability and accuracy, with explicit methods being more accurate and implicit methods being more stable. Our computational simulations also validated the hypothesis that myelination speeds up the propagation of action potentials. Finally, we showed that ephaptic coupling was possible in the EMI model

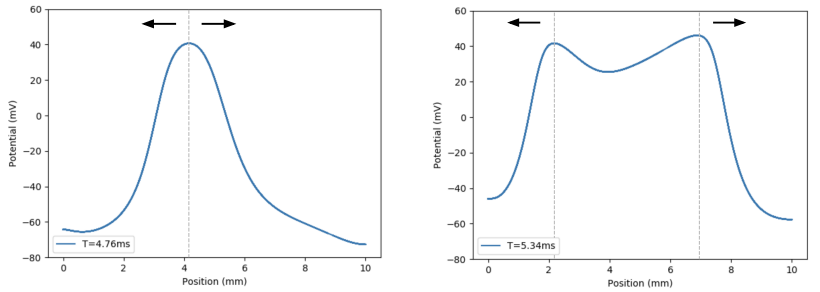

(a) *T=4.76ms*

(b) *T=5.34ms*

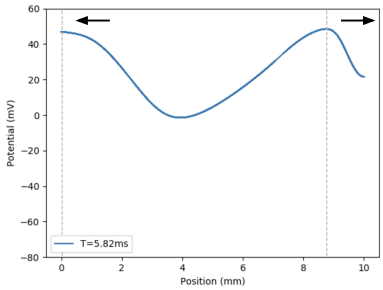

(c) *T=5.82ms*

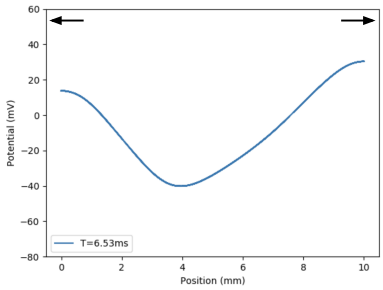

(d) *T=6.53ms*

Fig. 0.9: Action potentials induced in the central axon of the unmyelinated bundle for different time-stamps (sub-figures (a) through (d)). Arrows depict the splitting of the induced potential into forward and backward propagating impulses.

for both myelinated and unmyelinated axons, where myelination accelerated the propagation of the induced action potential.

Our work further supports the notion that biophysical models of excitable cells should take into account spatial geometry and dynamics to model more specialized biological phenomena. Both myelination and ephaptic coupling are important features of neuronal function and show pathology in disease, such as myelin loss in multiple sclerosis [20] or reduced ephpatic entrainment in neurodegenerative conditions [7]. For this reason, our report represents an important step towards complete models of excitable cells and the phenomena that can arise.

Although the EMI framework is a detailed and biophysically realistic model, further work using the more detailed KNP-EMI model [8], would allow for a more complete analysis of the parameters that modulate the emergence of induced action potentials, such as the distance between the axons in the bundle. Parameter values as measured in demyelinated axons could also be considered for modeling ephaptic coupling un-

der pathological conditions [15].

Furthermore, this report is a proof-of-concept showing that modeling ephaptic coupling and myelination is possible within this model, yet does not claim to replicate the exact dynamics seen in biological experiments. Further studies could confirm that the model outputs are consistent with theoretical predictions, that is, from the cable equation [5], or from experimental results.

References

1. C. A. Anastassiou and C. Koch. Ephaptic coupling to endogenous electric field activity: why bother? *Current opinion in neurobiology*, 31:95–103, 2015.
2. C. A. Anastassiou, R. Perin, H. Markram, and C. Koch. Ephaptic coupling of cortical neurons. *Nature Neuroscience*, 14(2):217–23, 2011.
3. A. Arvanitaki. Effects evoked in an axon by the activity of a contiguous one. *Journal of Neurophysiology*, 5(2):89–108, Mar. 1942. Publisher: American Physiological Society.
4. S. Binczak, J. C. Eilbeck, and A. C. Scott. Ephaptic coupling of myelinated nerve fibers. *Physica D: Nonlinear Phenomena*, 148(1):159–174, Jan. 2001.
5. H. Bokil, N. Laaris, K. Blinder, M. Ennis, and A. Keller. Ephaptic interactions in the mammalian olfactory system. *Journal of Neuroscience*, 21(20), 2001.
6. T. Brandt, M. Strupp, and M. Dieterich. Vestibular paroxysmia: a treatable neurovascular cross-compression syndrome. *Journal of Neurology*, 263(1):90–96, Apr. 2016.
7. G. M. Cunha, G. Corso, M. M. S. Lima, and G. Z. d. S. Lima. Electrophysiological damage to neuronal membrane alters ephaptic entrainment. *Scientific Reports*, 13(11974), 2023.
8. A. J. Ellingsrud, A. Solbrå, G. T. Einevoll, G. Halnes, and M. E. Rognes. Finite element simulation of ionic electrodiffusion in cellular geometries. *Frontiers in Neuroinformatics*, 14(11), 2020.
9. R. FitzHugh. Mathematical models of threshold phenomena in the nerve membrane. *The Bulletin of Mathematical Biophysics*, 17:257–278, 1955.
10. F. Fröhlich and D. A. McCormick. Endogenous Electric Fields May Guide Neocortical Network Activity. *Neuron*, 67(1):129–143, July 2010.
11. G. Grasso, A. Landi, and C. Alafaci. A Novel Pathophysiological Mechanism Contributing to Trigeminal Neuralgia. *Molecular Medicine*, 22(1):452–454, Jan. 2016. Number: 1 Publisher: BioMed Central.
12. E. Hairer and G. Wanner. *Solving Ordinary Differential Equations II: Stiff and Differential-Algebraic Problems*. Springer, 1996.
13. D. K. Hartline. What is myelin? *Neuron Glia Biology*, 4(2):153–63, 2008.
14. J. L. Hindmarsh and R. Rose. A model of neuronal bursting using three coupled first order differential equations. *Proceedings of the Royal Society of London. Series B. Biological Sciences*, 221(1222):87–102, 1984.
15. M. Hines and P. Shrager. A computational test of the requirements for conduction in demyelinated axons. *Restorative Neurology and Neuroscience*, 3(2):81–93, 1991.
16. A. L. Hodgkin and A. F. Huxley. A quantitative description of membrane current and its application to conduction and excitation in nerve. *Journal of Physiology*, 117(4), 1952.
17. J. G. Jefferys. Nonsynaptic modulation of neuronal activity in the brain: electric currents and extracellular ions. *Physiological Reviews*, 75(4):689–723, Oct. 1995. Publisher: American Physiological Society.
18. E. Kierig, J. Gerb, R. Boegle, B. Ertl-Wagner, M. Dieterich, and V. Kirsch. Vestibular paroxysmia entails vestibular nerve function, microstructure and endolymphatic space changes linked to root-entry zone neurovascular compression. *Journal of Neurology*, 270(1):82–100, Jan. 2023.

19. P. Morell and R. H. Quarles. *Basic Neurochemistry: Molecular, Cellular and Medical Aspects*. Lippincott-Raven, 6th edition, 1999.
20. M. Podbielska, N. L. Banik, E. Kurowska, and E. L. Hogan. Myelin recovery in multiple sclerosis: The challenge of remyelination. *Brain Sciences*, 3(3):1282–1324, 2013.
21. D. Purves, G. Augustine, and D. Fitzpatrick. *Neuroscience*. Sunderland, 2001.
22. G. Ruffini, R. Salvador, E. Tadayon, R. Sanchez-Todo, A. Pascual-Leone, and E. Santarnecchi. Realistic modeling of mesoscopic ephaptic coupling in the human brain. *PLOS Computational Biology*, 16(6):e1007923, June 2020. Publisher: Public Library of Science.
23. S. Rusch and H. Larsen. A practical algorithm for solving dynamic membrane equations. *IEEE Transactions on Biomedical Engineering*, 25:389–392, 1978.
24. H. Schmidt, G. Hahn, G. Deco, and T. R. Knösche. Ephaptic coupling in white matter fibre bundles modulates axonal transmission delays. *PLOS Computational Biology*, 17(2):e1007858, Feb. 2021. Publisher: Public Library of Science.
25. A. Tvieto, K. Jaeger, M. Kuchta, K.-A. Mardal, and M. E. Rognes. A cell-based framework for numerical modeling of electrical conduction in cardiac tissue. *Frontiers in Physics*, 5(48), 2017.
26. A. Tvieto, K.-A. Mardal, and M. E. Rognes. *Modeling Excitable Tissue: The EMI Framework*. Springer, 2021.